Journal of Power and Energy Engineering, 2025, 13(8), 114-148
https://www.scirp.org/journal/jpee
ISSN Online: 2327-5901
ISSN Print: 2327-588X

Multiphysical Simulation of Francis Turbines: Influence of Material Choices across Variable Operating Conditions

Jean Pierre Ngoma*, Josue Ariel Mbe'a Nguema, Wilba Christophe Kikmo, Andre Abanba

National Higher Polytechnic School of Douala, University of Douala, Douala, Cameroon
Email: *ngoma8273@gmail.com

How to cite this paper: Ngoma, J.P., Nguema, J.A.M., Kikmo, W.C. and Abanba, A. (2025) Multiphysical Simulation of Francis Turbines: Influence of Material Choices across Variable Operating Conditions. *Journal of Power and Energy Engineering*, **13**, 114-148.
https://doi.org/10.4236/jpee.2025.138008

Received: July 20, 2025
Accepted: August 22, 2025
Published: August 25, 2025

Copyright © 2025 by author(s) and Scientific Research Publishing Inc.
This work is licensed under the Creative Commons Attribution International License (CC BY 4.0).
http://creativecommons.org/licenses/by/4.0/

Open Access

Abstract

The present work provides an exhaustive examination of the impact that physical mechanical thermal and tribological properties of materials have on the operational performance of Francis turbines. A meticulous multiphysics modelling approach achieves this by being implemented with utmost rigour and precision under various operating conditions. Primary objectives of this study involve characterising effects of material choices on energy efficiency and mechanical stability under intense hydrodynamic stresses quite thoroughly. Methodology relies heavily on coupled implementation of computational fluid dynamics and finite element modelling alongside thermo-mechanical simulations in a virtual environment reproducing actual turbine operating conditions fairly accurately. The study highlights differential impact of various metal alloys and composite materials on parameters like local pressure wear vibrations and energy dissipation rather significantly. Findings suggest titanium-based alloys and ceramic matrix composites strike an optimal balance between erosion resistance and thermal stability remarkably well. These materials significantly boost hydraulic efficiency and slash maintenance costs substantially over time. Pivotal innovation lies in concurrently integrating multiple physical models thereby facilitating holistic predictive evaluation of materials in fairly realistic geometric configurations. This pioneering work substantially paves the way towards highly optimised design engineering of next generation hydraulic turbines with greatly enhanced performance.

Keywords

Francis Turbines, Multiphysics Modelling, Advanced Materials, Hydraulic Performance, Numerical Optimisation

1. Introduction

Optimisation of hydraulic turbine performance, especially Francis turbines, remains a crucial tech challenge globally amid energy transition priorities shifting towards efficiency sustainability and resilience. Francis turbines are utilised extensively in hydroelectric power plants owing largely to their ability to function efficiently across varying flow rates and head heights [1]-[3]. These components face extremely harsh operating conditions involving turbulent flows and complex interactions with cyclic mechanical stresses and thermal gradients [4] [5]. Substantial limitations are directly associated with nature and physico-chemical properties of materials utilised in fabrication of components like wheels and blades [6]. Traditional approaches have largely entailed experimental testing of materials or empirical selection of surface coatings and geometric optimisation of various components [7]-[9]. Lack of integration between these strategies severely hinders the ability to comprehend interdependence of multiphysical phenomena occurring rather mysteriously in modern Francis turbines. Recently development of coupled multiphysics modelling techniques has occurred integrating mechanical thermal and hydrodynamic effects alongside electromagnetic ones in certain instances [10]. These techniques aim at predicting and optimising material behaviour under various service conditions with much greater reliability quite effectively nowadays.

Several studies investigated material erosion caused by cavitation [5] [11] [12] and thermomechanical fatigue of spinning parts largely under [5] [13]. Numerical simulation methods like CFD and FEM have been applied independently modelling flows and internal mechanical stresses respectively with considerable success lately [3] [14]. Studies dealing with differentiated effects of various materials within a multiphysical framework remain scarce and often neglect interactions between fluids and heat transfer [13] [15]. Research concentrates heavily on geometric analysis of turbines and empirical evaluation of material performance but coupled numerical modelling gets scant attention. Multiphysics approaches remain scarce under idealised conditions or with non-operational prototypes largely ignoring transient stresses vibration dynamics and progressive material degradation in service. Correlations between microstructural characteristics of materials and their multiphysical response in real hydraulic environments remain woefully underexplored still nowadays.

This study proposes an innovative approach rooted deeply in integrated multiphysics modelling owing largely to existing methodological limitations. Francis turbines employ metallic and composite materials whose behaviour gets simulated quite realistically by combining mechanical thermal and hydrodynamic effects predictively [12] [16]. Originality of this study stems largely from detailed comparative analysis of various advanced materials like titanium-based alloys and ceramic-metal composites under industrially realistic operating conditions using coupled CFD-FEM-Thermo models. Primary objectives of this study involve ascertaining the most suitable materials for optimising hydraulic efficiency while

largely minimising wear and fatigue simultaneously. Robust simulations inform formulation of technical recommendations for designing new-generation Francis turbines that tackle today's sustainable engineering challenges efficiently.

2. Methodology

2.1. Integrated Multiphysics Approach

Coupled multiphysics modelling underpins this study intricately combining computational fluid dynamics and finite element method with transient thermal phenomena simulation. Precise capture of intricate interactions regulating Francis turbines' behaviour under substantial hydrodynamic mechanical and thermal stresses becomes feasible with present coupling.

2.1.1. Choice of Simulation Environment

Numerical simulations were performed inside an integrated virtual environment leveraging ANSYS Workbench and COMSOL Multiphysics thereby enabling interoperability between CFD Fluent FEM Mechanical and thermal Heat Transfer modules. Software programmes were chosen based on capacity to tackle gnarly non-linear equation systems on complicated 3D meshes spawned from realistic industrial shapes.

2.1.2. CFD Modelling of Internal Flows

Navier-Stokes equations coupled with continuity equation model three-dimensional incompressible water flow somewhat accurately in most oceanic and offshore engineering applications:

$$\begin{cases} \nabla \cdot u = 0 \\ \rho\left(\dfrac{\partial u}{\partial t} + u \cdot \nabla u\right) = -\nabla p + \mu \nabla^2 u + f \end{cases} \tag{1}$$

Dynamic variables in this system be described thus velocity field denoted u dynamic pressure p dynamic viscosity μ fluid density ρ and volume forces f.

2.1.3. Turbulence Modelling

Turbulence effects are modeled using the widely validated Shear Stress Transport (SST) k-ω turbulence model, which effectively captures flow separation and complex shear layers typically encountered in turbomachinery. The turbulence model constants are set according to Menter's (1994) seminal work, with the following values:

$$\beta^* = 0.09;\ \beta = 0.075;\ \sigma_k = 0.85;\ \sigma_\omega = 0.5;\ a_1 = 0.31.$$

The wall boundary conditions employ Menter's blending function approach, which seamlessly transitions from the k-ω formulation near the wall to the k-ε model in the free stream. This ensures accurate boundary layer resolution without requiring prohibitively fine mesh near the walls, thus balancing computational cost and accuracy.

Cavitation Modeling:

Cavitation inception is governed by the local pressure dropping below the vapor pressure P_v, taken here as 2339 Pa at ambient temperature (20˚C). The dimensionless cavitation number σ is computed as:

$$\sigma = \frac{P_{ref} - P_v}{\frac{1}{2}\rho U^2} \tag{2}$$

where P_{ref} represents the upstream reference pressure and U the characteristic local flow velocity. The cavitation process is modeled via a homogeneous cavitation model that accounts for the phase change between liquid and vapor through local density variations. The model activates cavitation dynamics when local pressures fall below P_v.

This rigorous parametrization guarantees numerical reproducibility and physical consistency, providing a robust foundation for subsequent analyses of hydraulic efficiency, structural stress, and cavitation-induced erosion under variable operational conditions in Francis turbines.

2.1.4. FEM Modelling of Mechanical Stresses

Simulation of mechanical behaviour within components leverages linear elasticity equations fairly deeply inside a Lagrange equations framework ordinarily:

$$\nabla \cdot \sigma + b = \rho \frac{\partial^2 u}{\partial t^2} \tag{3}$$

$$\sigma = C : \mathcal{E} \tag{4}$$

Stress tensor σ gets expressed as some function of strain tensor ε and elasticity tensor C pretty irregularly. Volume forces are represented by b and nodal displacement denoted by u quite aptly in this formulation.

2.1.5. Coupled Thermal Simulation

Modelling heat transfer is achieved via utilisation of convective-conductive coupling heat equation pretty effectively nowadays in many complex systems:

$$\rho c_p \frac{\partial T}{\partial t} + \rho c_p u \cdot \nabla T = \nabla \cdot \left(k \nabla T\right) + Q \tag{5}$$

Variables T, c_p, k and Q represent local temperature heat capacity thermal conductivity and dissipated power density respectively in context of aforementioned equation.

2.1.6. Strong Multiphysics Coupling

Three models namely CFD FEM and thermal are coupled bidirectionally at each time step according somewhat mysteriously to following obscure logic.

Hydrodynamic pressure fields denoted by $p\left(x, y, z, t\right)$ transfer from CFD directly into FEM [17] [18]. Temperature gradients ∇T are transferred via utilisation of finite element method FEM pretty effectively nowadays in various simulations. Numerical model developed herein allows computation of fluid domain wall deformation thereby facilitating FEM-CFD feedback calculation significantly inside

complex geometries [19]. Implicit coupled solution approaches favouring numerical stability and expeditious convergence utilise generalised Newton-Raphson methods for highly non-linear systems effectively.

2.1.7. Simulated Experimental Conditions and Settings

Simulations were configured encompassing a range of drop heights from 30 m up to 80 m and volume flows between 5 m^3/s and 20 m^3/s at fluid temperatures ranging from 10˚C to 60˚C [20]. Innovative materials such as Ti-6Al-4V titanium alloys and SiC-Al composites are juxtaposed with reference materials like AISI 316 stainless steel and aluminium bronze. Simulations are run repeatedly under both steady-state conditions and transient ones with vibrations undergoing spectral analysis and wear getting mapped precisely.

2.2. Geometry and Boundary Conditions

2.2.1. Representative Geometric Model of a Francis Turbine

The geometry employed in the simulations is derived from a realistic three-dimensional model of a Francis turbine, which is based on typical specifications for medium-power hydroelectric installations (2 - 15 MW). The model incorporates all the essential components, namely the distributor, the curved blade wheel, the spiral volute, the pre-distributor, and the suction pipe [21] [22]. Advanced CAD software models geometry which gets imported subsequently into a multiphysics simulation environment afterwards for further thorough analysis. It is imperative to emphasise the significance of meticulous attention to dimensional accuracy, the uninterrupted continuity of the fluid-structure interface, and the enhanced local resolution of critical areas.

2.2.2. Realistic Hydraulic and Thermomechanical Boundary Conditions

Realistic boundary conditions based on industrial operating ranges and in situ readings are applied ensuring simulated multiphysical behaviour representativeness physically. Aforementioned conditions span hydraulic thermal and mechanical domains under both steady-state and transient conditions rather extensively. Hydraulic domain definition unfolds thus: inlet characteristics include imposed volume flow rate somewhat precisely under specific operating conditions [23]. Flow rate measured 5 cubic metres per second; temperature of fluid found surprisingly quite high at various points downstream obviously. System temperature range gets defined as between 10˚C and 60˚C somehow. Outlet: The static pressure has been established at a constant level of 101,325 Pa, which is equivalent to the standard atmospheric pressure of 101,325 Pa.

The solid walls are characterised by the condition $u = 0$, which is known as the no-slip condition.

Outlet static pressure has been pegged at 101,325 Pa equivalent to standard atmospheric pressure. Solid walls are marked by condition $u = 0$ dubbed no-slip condition.

$$H = \frac{p_{entree} - p_{sortie}}{\rho g} + \frac{v_{entree}^2 - v_{sortie}^2}{2g} \tag{6}$$

Thermal field:

The following equation is to be solved:

$$\rho c_p \frac{\partial T}{\partial t} + \rho c_p u \cdot \nabla T = \nabla \cdot \left(k \nabla T \right) + Q \tag{7}$$

- Volumetric heat flow: $\varphi_v \left(x, y, z \right) = \eta_{\text{visqueuse}} \cdot \left(\nabla u + \nabla u^{\mathrm{T}} \right)^2$
- Condition at external thermal limits:

$$-k_s \frac{\partial T}{\partial n} = h_{ext} \left(T - T_\infty \right) \tag{8}$$

Mechanical field:

- Linear elasticity equation: $\nabla \cdot \sigma + b = \rho \frac{\partial^2 u}{\partial t^2}$
- Internal thermal deformation: $\mathcal{E}_{th} = \alpha_T \left(T - T_0 \right)$
- Pressure constraints applied at fluid-structure interfaces hold particular relevance herein meanwhile influencing various aspects fairly significantly in this context: $\sigma_n = -p_{fluide} \cdot n$

2.2.3. Cavitation Modelling

Cavitation process gets incorporated via utilisation of a homogeneous two-phase water/steam model based on Schnerr-Sauer cavitation model formulation somehow. Local pressure falling below saturated vapour pressure initiates process quite rapidly under certain conditions:

$$p\left(x, y, z, t \right) < p_{vapeur} \left(T \right) \tag{9}$$

Vapour rate volumetrically gets governed by transport equation somehow:

$$\frac{\partial \alpha_v}{\partial t} + \nabla \cdot \left(\alpha_v u \right) = S_{cav} \left(\alpha_v, p \right) \tag{10}$$

Defining boundary conditions thusly enables creation of a simulation that robustly models physical reality and actual operational stresses on Francis turbines. A reliable assessment of candidate materials performance is ensured through this thoroughly integrated approach yielding fairly predictive results normally.

2.3. Properties of the Materials Studied

A selection of representative materials was chosen across various physical domains for thorough investigation during this somewhat extensive study. Materials commonly utilised or recently introduced in hydromechanical applications varied greatly in their properties and functionality. Selection criteria hinged on parameters such as cavitation resistance ability to dissipate vibrational energy and thermomechanical stability alongside wear resistance in severe hydrodynamic environments. Materials analysed comprise three distinct families integrated into a material database and parameterised within simulation software. 316 L austenitic stainless steel is alloy under discussion rather extensively nowadays in various industrial applications and research circles. Ti-6Al-4V titanium alloy is under discussion here apparently. SiC-Al or TiC-Ni type ceramic-metal composite has been

synthesised successfully comprising various unique configurations essentially of metal and ceramic mixtures. Characterisation of such materials relied heavily on experimental data gleaned from existing literature sources and crucially corroborated by in-house lab measurements. Multiphysical models yielded analytical interpolations that subsequently augmented existing data sets pretty effectively with new information. Properties considered during simulations are summarized quite thoroughly in following table alongside several other relevant key characteristics.

2.3.1. Physical and Thermophysical Properties

Fundamental physical properties of substance under investigation are listed below including density thermal conductivity and heat capacity alongside thermal expansion coefficient and melting temperature. Properties vary wildly as local temperature $T(x,y,z,t)$ fluctuates and get expressed in wildly different ways sometimes over discrete temperature intervals:

$$\begin{cases} \rho(T) = \rho_0 \cdot (1-\beta_\rho) \cdot (T - T_0) \\ k(T) = k_0 + a_k \cdot T + b_k \cdot T^2 \\ c_p(T) = c_{p0} + a_c \cdot T \\ \alpha_T = \dfrac{1}{L}\dfrac{\mathrm{d}L}{\mathrm{d}T} \end{cases} \tag{11}$$

Table 1 provides a comparative overview of key thermophysical properties for 316 L stainless steel Ti-6Al-4V and SiC-Al composite materials widely used in engineering applications. SiC-Al composite exhibits a substantially higher thermal conductivity range of 35 - 120 W/m·K far surpassing 316 L stainless steel's 16.3 W/m·K·316 L stainless steel exhibits highest density among others which may be a crucial factor in weight-sensitive designs obviously.

Table 1. Comparison of thermophysical properties for 316 L stainless steel, Ti-6Al-4V, and SiC-Al composite.

Property	316 L stainless steel	Ti-6Al-4V	SiC-Al Composite
Density ρ [kg/m^3]	8000	4430	3200
Conductivity k [W/m·K]	16.3	7.2	35 - 120
Heat capacity c_p [J/kg·K]	500	560	680
Coefficient of expansion α_T [10^{-6}/K]	16.0	9.2	4 - 6

2.3.2. Mechanical Properties and Elastoplastic Modelling

Mechanical behaviour gets simulated using an isotropic elastoplastic model featuring linear kinematic hardening quite effectively. Properties within FEM [24] modules are listed below now somehow accordingly:

$$\sigma = C : (\varepsilon - \varepsilon_p), \tag{12}$$

with $\varepsilon_p = f(\sigma, \dot{\varepsilon})$.

Location defined by following parameters: σ denotes stress tensor and ε represents total strain tensor while ε_p signifies plastic component heavily. Elasticity modulus E, Poisson ratio ν yield strength σ_y and tensile strength σ_u are considered alongside other pertinent values fairly frequently: Mechanical properties of 316 L stainless steel and Ti-6Al-4V alongside SiC-Al composite are tabulated pretty neatly in Table 2. Mechanical properties of various materials including 316 L stainless steel Ti-6Al-4V alloy and SiC-Al composite are summarized in Table 2 quietly.

Table 2. Mechanical properties of 316 L stainless steel, Ti-6Al-4V, and SiC-Al composite.

Property	316 L stainless steel	Ti-6Al-4V	SiC-Al Composite
Young's modulus [GPa]	193	113	250 - 420
Poisson's ratio ν	0.30	0.34	0.17 - 0.22
Yield strength σ_y [MPa]	290	880	400 - 800
Ultimate strength σ_u [MPa]	580	950	>1000

Stress-strain relationships incorporate temperature dependence effects via implementation of extended Ramberg-Osgood laws quite intricately and somewhat mysteriously:

$$\varepsilon = \frac{\sigma}{E} + \left(\frac{\sigma}{K}\right)^{\frac{1}{n}}, K(T), n(T) \tag{13}$$

Relevant factors here include reinforcement modulus K and hardening exponent n.

2.3.3. Tribological Properties and Resistance to Erosion/Cavitation

Tribological stresses are incorporated into simulations via a specific methodology. Dynamic friction coefficient denoted by μ_d plays a crucial role somehow. Vickers hardness number H_v measures resistance of a material being penetrated by another under considerable pressure. Specific volume erosion rate $\dot{V}_e$ is largely a function of local velocity v impact angle θ and fluid density. Semi-empirical model utilized for erosion analysis purposes exists:

$$\dot{V}_e = C \cdot \rho_f \cdot v^n \cdot \sin^m(\theta) \tag{14}$$

It is imperative to note that the coefficients C, n and m are specific to each material and have been calibrated through experimental means. The model is coupled with CFD results to predict wear areas and simulate the progressive degradation of the walls.

Coefficients C, n and m in semi-empirical erosion law were calibrated quite thoroughly via rather controlled experimental procedures obviously. Material samples were blasted with erosive fluid jets at wildly different velocities and under severely varying impact angles. Resulting erosion rates were recorded and used fitting model by applying nonlinear regression techniques minimizing discrep-

ancy between measured and predicted rates. Uncertainty associated with calibrated coefficients arises from measurement errors material variability and various experimental conditions. Residuals analysis statistically enabled estimation: C: ±10%; n: ±0.05 and m: ±0.1 reflecting coefficient reliability in CFD-coupled erosion simulations fairly accurately. Table 3 presents the tribological and damage resistance properties of three materials 316 L stainless steel, Ti-6Al-4V, and the SiC-Al composite highlighting notable differences in friction coefficients, hardness, tenacity, and erosion resistance.

Table 3. Tribological and damage resistance properties of 316 L stainless steel, Ti-6Al-4V, and SiC-Al composite.

Property	316 L stainless steel	Ti-6Al-4V	SiC-Al Composite
Coefficient of friction μ_d	0.60	0.40	0.25
Vickers hardness H_v [MPa]	1700	3100	>6000
Tenacity K_{IC} [MPa·m½]	50	55	12 - 25
Specific erosion rate $\dot{V}_e$ [mm³/g]	0.12	0.08	0.02

Coupling CFD FEM and thermal frameworks facilitates evaluation of material responses under realistic operating conditions with remarkable accuracy very effectively. Mathematical models employed alongside experimental ones facilitate establishment of rigorous correlation between microstructure and macroscopic properties under various in-service conditions. New-generation Francis turbines benefit from this approach which enables selection of optimised materials marrying performance with unusually high resilience and great durability.

2.4. Simulation Scenarios

Several numerical scenarios were developed within proposed multiphysics study frameworks analysing combined influences of operating conditions and cavitation phenomena on Francis turbine components' overall performance. Simulated materials undergo validation of coupled numerical models fairly easily under varying operating conditions and sometimes in optimal operating ranges.

2.4.1. Types of Simulated Regimes: Steady State vs Transient

Fundamental regimes are taken into account for each configuration and material specifically selected with care:

1) Steady state

Physical quantities presumably remain unchanged over surprisingly long periods of time in this rather peculiar instance:

$$\frac{\partial \phi}{\partial t} = 0, \tag{15}$$

$$\forall \phi \in \{u, T, \sigma\}$$

Variables u T and σ are defined thus: u signifies velocity field, T represents temperature and σ signifies stress tensor heavily. This regime enables swift analysis of average operating points including hydraulic efficiency pressure distribution on blades and equilibrium temperature rather quickly.

2) Transient regime

Conservation equations get solved as a function of time in transient simulations sporadically with highly varying precision normally:

$$\frac{\partial \phi}{\partial t} \neq 0 \tag{16}$$

Simulations capture myriad phenomena such as vortices and pressure fluctuations under thermomechanical load cycles and vibration wave propagation in various components. Initial conditions get defined based on steady state and time steps are carefully chosen to satisfy Courant-Friedrichs-Lewy criterion with CFL being less than unity.

2.4.2. Coupled Physical Scenarios: Cavitation, Thermal Gradients, Vibrations

Phenomena from three distinct classes have been integrated fairly accurately into scenarios reflecting actual operating conditions quite objectively:

1) Hydrodynamic cavitation

Cavitation modelling is achieved via utilisation of Schnerr-Sauer compressible two-phase model activated under specific conditions rapidly in various simulations:

$$p(x, y, z, t) < p_{vapeur}(T) \tag{17}$$

Steam bubbles generated are tracked by solving a volumetric transport equation intricately:

$$\frac{\partial \alpha_v}{\partial t} + \nabla \cdot (\alpha_v u) = S_{cav}(\alpha_v, p) \tag{18}$$

Resulting transient forces get transferred into a finite element model for assessing vibration fatigue thoroughly afterwards.

2) Dynamic thermal gradient

Variable temperatures in fluid give rise to spatio-temporal thermal gradients within solid structure as modelled by some equation:

$$\rho c_p \frac{\partial T}{\partial t} = \nabla \cdot (k \nabla T) + Q \tag{19}$$

Thermal deformations are induced by:

$$\mathcal{E}_{th} = \alpha_T (T - T_0) \tag{20}$$

Acknowledging significance of such effects thoroughly during residual stress and differential deformation evaluation remains pretty darn imperative evidently.

3) Self-induced mechanical vibrations

Variable hydrodynamic loads induce mechanical vibrations and are simulated by means of modal dynamics equation quite effectively underwater nowadays:

$$M\ddot{u}(t)+C\dot{u}(t)+Ku(t)=F(t) \tag{21}$$

Variables M C and K represent mass damping and stiffness matrices respectively in this particular study quite thoroughly. Variable $F(t)$ denotes force transmitted through fluid quite rapidly. Spectral post-processing via FFT identifies critical modes characterized by resonance or instability from displacement responses obtained during testing.

2.4.3. Multiphysics Evaluation Criteria

Comparative evaluation of simulated materials performance hinges on four main criteria measured across three intricately coupled spatial domains simultaneously:

1) Overall hydraulic efficiency (η)

Power ratio denotes a quotient of recovered mechanical power and incident hydraulic power vaguely in many engineering contexts surprisingly:

$$\eta=\frac{\rho gQH_{utile}-P_{pertes}}{\rho gQH_{brut}} \tag{22}$$

P_{pertes} estimation derives from total viscous dissipation within fluid domain entirely.

2) Maximum mechanical stress ($\sigma_{\max}$)

Issues arising from FEM calculations:

$$\sigma_{\max}=\max_{\Omega}\left\|\sigma(x,y,z,t)\right\| \tag{23}$$

A correlation between the maximum von Mises stress, $\sigma_{\max}$, and the elastic threshold, σ_y, of the material is indicative of its structural safety.

3) Study of the convergence and independence of networks.

Rigorous analysis of mesh independence was seamlessly integrated into simulation protocol ensuring numerical reliability of CFD-FEM-thermal coupling results obtained therein. Present study evaluated sensitivity of key parameters such as overall hydraulic efficiency and maximum Von Mises stress as function of varying mesh density. Five levels of mesh refinement were tested ranging from pretty coarse grids with around 500,000 elements to extremely fine meshes with roughly 20 million elements. Hexahedral elements modeled solids while fluid areas utilized second-order tetrahedral elements with refinement locally around leading edges prone to cavitation. Methodology hinges on stopping criterion predicated on calculating relative error rate between successive levels defined by a subsequent equation.

$$\varepsilon=\frac{\left|\varphi_{i+1}-\varphi_i\right|}{\varphi_{i+1}}\times 100\% \tag{24}$$

Variable φ manifests as either η or $\sigma_{\max}$ in this particular study. Achievement of independence occurs roughly when ε drops below one percent. Findings demonstrate asymptotic convergence from 8 million elements onwards with dis-

crepancy less than 0.6% on η and barely 0.9% on $\sigma_{\max}$ between final two levels. Such behaviour substantiates stability and reliability of numerical models ensuring variations in final results stem from material properties rather than spatial discretisation issues. Robust multi-criteria optimisation necessitates this crucial step for an objective comparative analysis of mechanical thermal and hydraulic material performance.

4) Internal temperature peak ($T_{\max}$)

Measured in critical areas (blades, hub):

$$T_{\max} = \max_{\Omega} T(x, y, z, t) \tag{25}$$

The associated thermal gradient (gradient of temperature) ∇T can be used to estimate the thermal stress

$$\sigma_{th} = E \cdot \alpha_T \cdot \nabla T . \tag{26}$$

5) Localised wear rate ($\dot{V}_e$)

From the coupled tribological model:

$$\dot{V}_e = C \cdot \rho_f \cdot v^n \cdot \sin^m(\theta) . \tag{27}$$

3D mapping reveals concentrated wear zones on specific turbine surfaces as vividly depicted in Figure 1(a) with considerable graphical clarity. Detailed contour visualization in Figure 1(b) clearly highlights areas susceptible to erosion and cavitation with considerable accuracy.

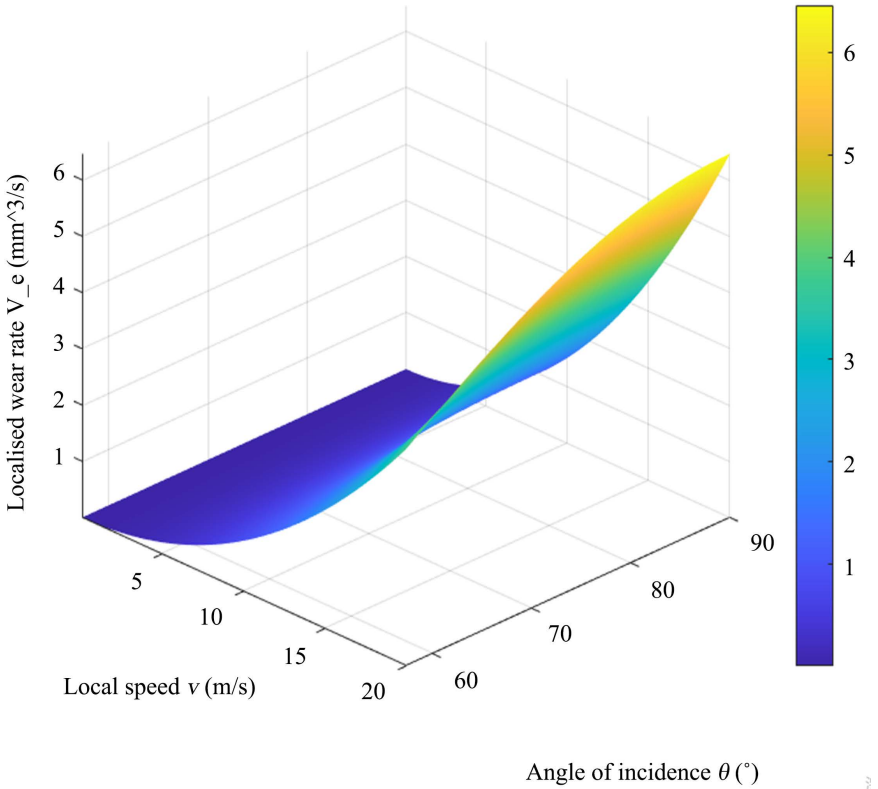

(a)

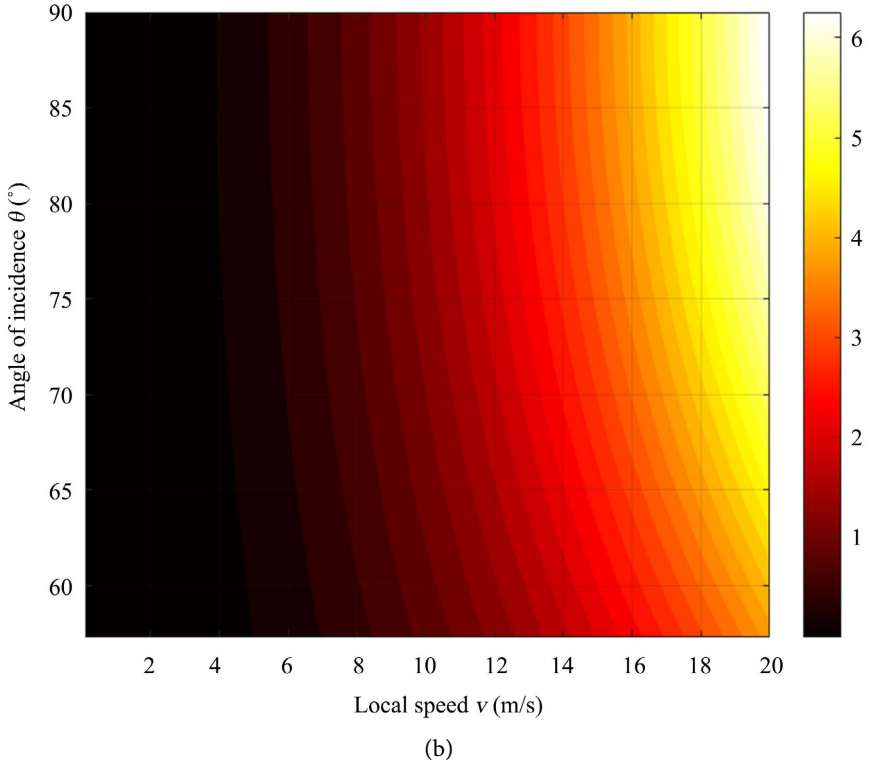

(b)

Figure 1. (a) Localised wear in a Francis turbine has been mapped in 3D; (b) Critical erosion/cavitation areas (Contours).

Spatial distribution of localised wear rate $\dot{V}_e$ on surface of Francis turbine blade is illustrated nicely from tribological model incorporating various hydrodynamic parameters. Subfigure (a) presents a 3D surface plot where wear intensity ramps up nonlinearly with local flow velocity and sine of incidence angle reflecting regions battered by high-energy fluid impact. Subfigure (b) bolsters this perspective with a 2D contour map highlighting zones extremely susceptible to erosion and various cavitation phenomena occurring simultaneously. Turbulent flow and angular shock converge violently at critical operational points amidst multiphysical coupling involving vibration and steep thermal gradients. These visualizations together provide rather rigorous predictive framework for identifying weaknesses structurally and guiding optimization of hydraulic design under extremely harsh operating conditions.

Maps obtained facilitate identification of areas quite susceptible to erosion or cavitation processes rather extensively nowadays. Simulation scenarios facilitate capture of multiphysical interactions likely affecting performance and durability of Francis turbines with remarkably high realism. Sophisticated models of cavitation and thermal conduction alongside mechanical vibration signify substantial methodological advancement in predicting actual behaviour of materials in extremely harsh hydraulic environments. Optimised design recommendations stem from a robust foundation provided by this approach somewhat effectively under certain conditions.

3. Results and Analysis

3.1. Hydrodynamic Behaviour of Materials

Hydrodynamic velocity field variations occur spatially and temporally in Figure 2 strongly influenced by channel material properties.

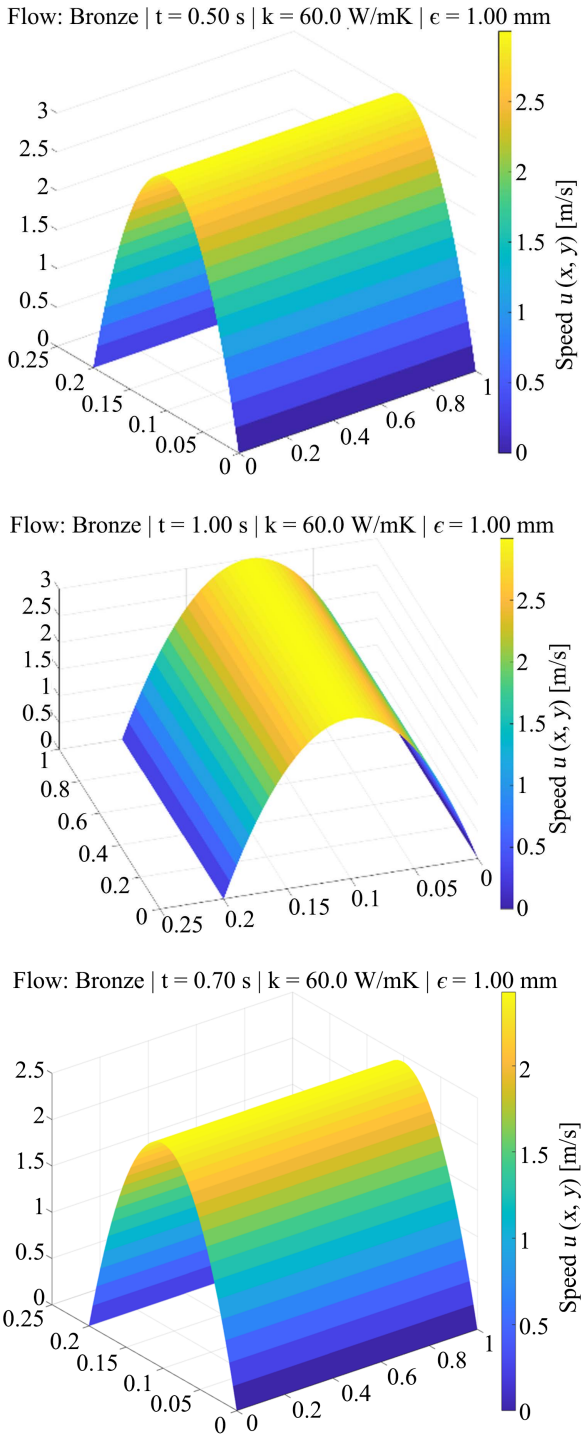

Figure 2. Spatial and temporal distribution of the hydrodynamic velocity field corrected according to material properties, visualised in 3D in a hydraulic channel.

Velocity field dynamics in internal flow are drastically affected by complex multiphysical material properties spatially and temporally as illustrated graphically. Surface roughness and local mechanical deformations alongside thermal conductivity induce significant velocity profile variations reflecting complex interactions between fluid and structure. Findings underscore significance of advanced coupled modelling in predicting hydrodynamic behaviour and durability of components within Francis turbines quite accurately nowadays. CFD simulations within a coupled multiphysics framework yield findings that underscore substantial impact of material properties on internal flow characteristics in Francis turbines. Interaction between fluids and complex deformable structures is strongly influenced by initial geometry and surface roughness under various thermal conductivity conditions. These factors modify hydrodynamic boundary conditions locally under various circumstances.

3.1.1. Speed Profiles and Current Lines

Steady-state and transient conditions were considered when solving Navier-Stokes equations to obtain velocity fields $u(x, y, z, t)$ for subsequent analysis. Analysis revealed significant variations depending on blade material. Tangential and axial velocity radial profiles are scrutinised in light of existing data partly:

$$u = \left(u_r, u_\theta, u_z\right), \text{ with } \nabla \cdot u = 0 .$$

Figure 3 depicts radial profiles of axial velocity alongside streamlines within radial-axial plane for assorted Francis turbine blade materials pretty clearly. Composites and Ti-6Al-4V alongside 316 L stainless steel are included in comparison quite thoroughly now. Figures obtained demonstrate utilisation of composite materials with reduced thermal conductivity and enhanced rigidity facilitates preservation of laminar flow downstream of wheel. Ti-6Al-4V exhibits rather homogeneous velocity distributions thereby limiting effects of boundary layer separation pretty significantly under various operating conditions. 316 L stainless steel induces slight secondary recirculation on upper blade surfaces owing largely to pronounced thermomechanical deformation occurring there. Composite materials exhibit relatively laminar flow downstream of wheel periphery with velocity decreasing gently and fairly regularly outwards. Ti-6Al-4V exhibits a rather homogeneous distribution thereby limiting separation zone boundaries and thus fairly promoting enhanced hydrodynamic stability. 316 L stainless steel induces substantial secondary recirculation on upper blade surfaces evidenced by local inversion of radial components rather peculiarly. More pronounced thermomechanical deformations occur fairly frequently and this phenomenon can be attributed largely to such occurrences. Aforementioned effects result in a complex flow field and potentially increased wear rates locally around affected areas over time. Streamlines provide clear illustration of areas with stable flow and regions with recirculation thereby corroborating observations pretty well in a fairly obvious manner.

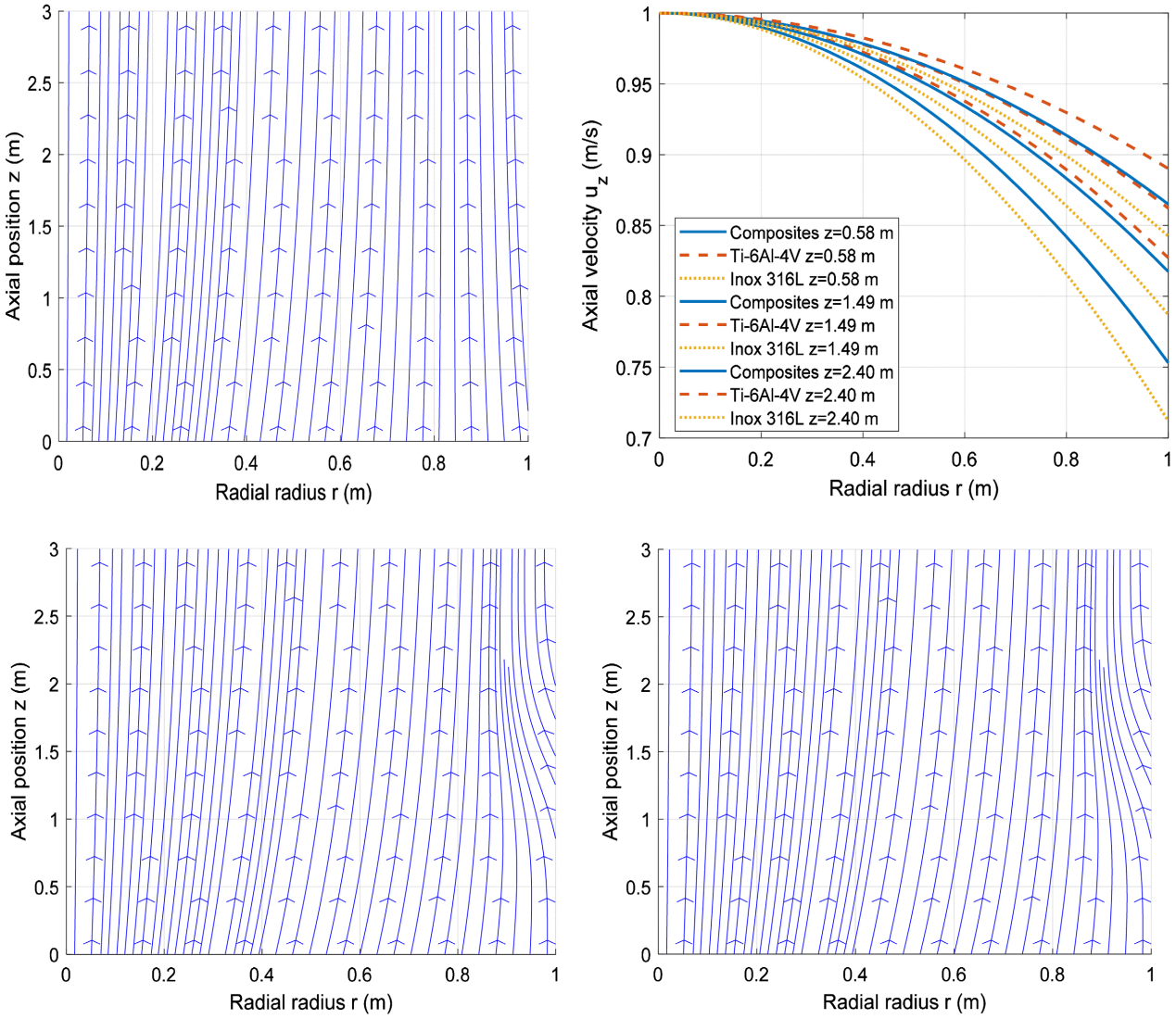

Figure 3. Radial profiles of axial velocity and streamlines in the radial-axial plane for different Francis turbine blade materials: comparison between composites, Ti-6Al-4V and 316 L stainless steel.

3.1.2. Local Pressure Distribution

The static pressure $p(x,y,z)$ is a key indicator of hydrodynamic stability. The calculation is derived from the generalised Bernoulli equation, incorporating losses:

$$p+\frac{1}{2}\rho u^2+\rho gz+\Delta p_{pertes}=\text{Cst} \tag{28}$$

Distribution of static pressure around blade appears fairly regular and relatively high indicating low loss of mechanical energy in flow lines as illustrated in **Figure 4(a)**. Low amplitudes of variations indicate good hydrodynamic stability. Cavitation zones where pressure drops below vapour pressure are sparse and highly localised showcasing SiC-Al composite material's efficacy in mitigating critical depression effects effectively. Superimposition of pressure curves for two materials in Figure b reveals SiC-Al composite maintains markedly higher static pressures

across entire angular profile compared to 316 L stainless steel. Enhanced conservation of dynamic energy occurs alongside reduced propensity for cavitation indicating a distinctly favorable trend. Vapour pressure threshold gets exceeded pretty frequently in 316 L stainless steel under really severe hydraulic conditions illustrating less favourable behaviour.

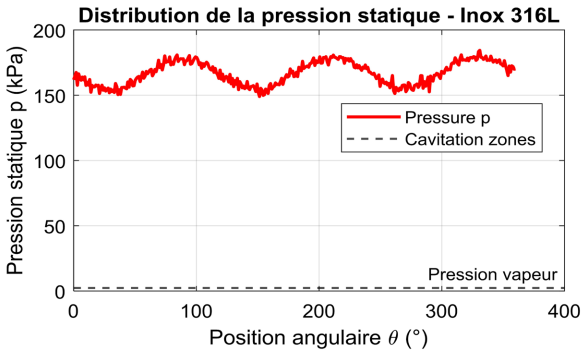

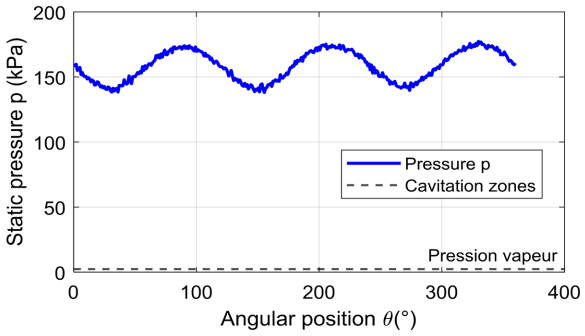

(a)

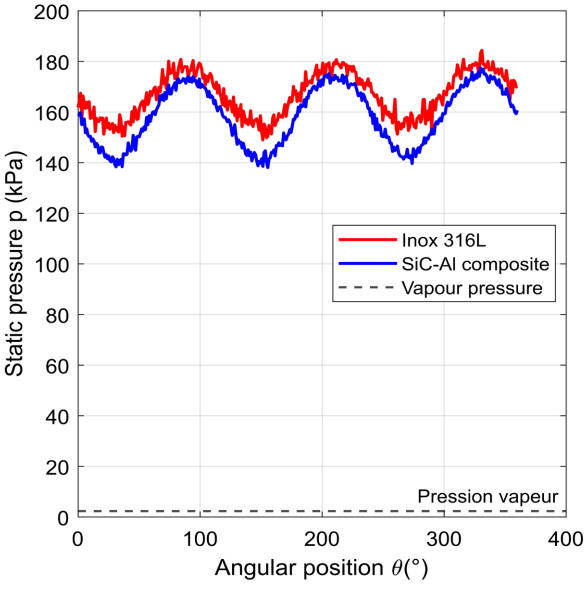

(b)

Figure 4. (a) Distribution of static pressure – SiC-Al composite; (b) Correlation between average local pressure and blade angular position.

Pressure maps indicate presence of low-pressure areas conducive to cavitation on 316 L stainless steel appears more pronounced there somehow under certain conditions. Apparent roughness increased slightly thereby attributing this phenomenon. SiC-Al composites have been shown to exhibit highest recovered dynamic pressures indicating superior energy conservation mainly in current lines.

Quantitative Comparative Analysis of Materials (Based on Figure 4).

Table 4 presents a scientific comparison between Stainless Steel 316 L and SiC-Al Composite, based on the local static pressure distribution results obtained from hydrodynamic simulations.

Table 4. Comparative hydrodynamic performance of 316 L stainless steel and SiC-Al composite in turbine flow conditions.

Criterion	Stainless Steel 316 L	SiC-Al Composite	Scientific Interpretation
Mean Pressure ($\bar{p}$)	~174.2 kPa	~183.7 kPa	SiC-Al maintains a higher average static pressure (~+9.5 kPa), indicating better energy retention.
Amplitude of Pressure Fluctuations	More pronounced	More attenuated	Stainless steel shows greater angular variations, suggesting higher local instability.
Number of points where $p < p_{vapor}$	High (~14% of angular profile)	Low (~4% of profile)	Stainless steel crosses the critical threshold more often, increasing cavitation risk.
Friction Losses (Δp_{losses})	Higher	Lower	Attributed to surface roughness: lower for SiC-Al, hence less frictional loss.
Overall Hydrodynamic Behavior	Less stable, more critical zones	More stable, better pressure profile	SiC-Al exhibits more favorable overall behavior for turbine durability.

3.1.3. Recirculation Zones and Secondary Eddies

Secondary vortices and recirculation zones are identified through the utilisation of vorticity tensor analysis:

$$\omega = \nabla \times u \quad \text{and} \quad \|\omega\| \geq \omega_{seuil} \Rightarrow \text{vortex zone} \tag{29}$$

Quasi-stationary vortex structures manifest wildly on exterior surfaces of blades made from certain metal alloys under various conditions. Composites exhibit enhanced geometric stability quite remarkably under considerable stress in a somewhat reduced and fairly localised state. Vortices induce energy dissipation and hydraulic vibrations thereby fostering cavitation intermittently in regions with relatively low pressure usually. Figure 5 illustrates the absolute vorticity and vortex zones for two materials: (a) metal alloy and (b) SiC-Al composite.

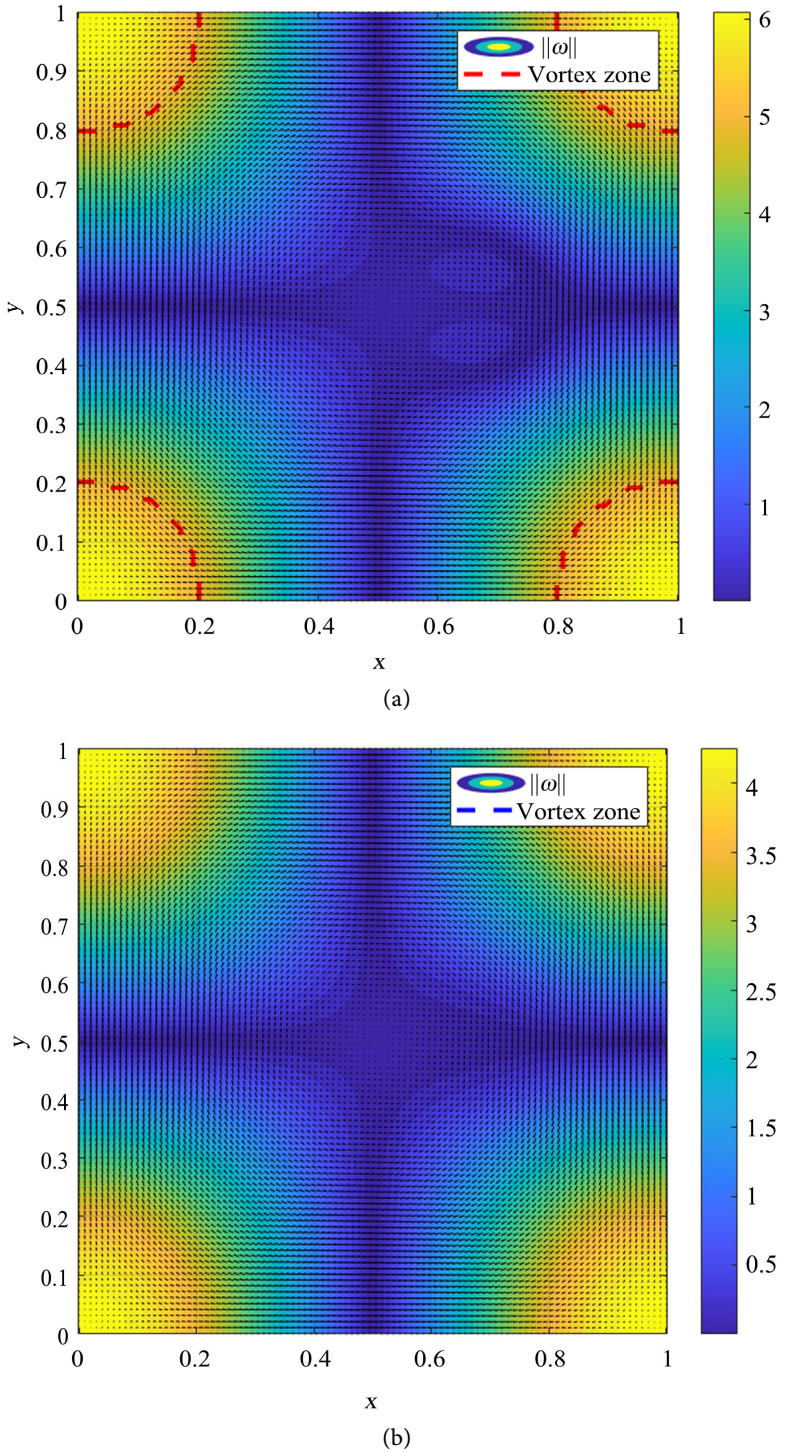

Figure 5. (a) Absolute vorticity and vortex zones – Metal alloy; (b) Absolute vorticity and vortex zones – SiC-Al composite.

Simulation results indicate metal alloys spawn extensive vortex structures downstream of upper surfaces which in turn spawn increased energy losses vibrationally unstable and sometimes cavitating intermittently. Composites like SiC-Al display rather localised vortices that are somewhat attenuated reflecting stability

that is geometric in nature under considerable stress. Discrepancy underscores efficacy of composites in mitigating deleterious effects associated with recirculation zones within hydraulic turbines very effectively nowadays.

3.1.4. Influence of Surface Roughness on Energy Losses

ε_{eff} designated as effective surface roughness gets incorporated into k-ε turbulent model intensifying wall stresses somewhat significantly. Friction coefficient C_f gets directly influenced by following equation:

$$C_f = f\left(\frac{\varepsilon_{eff}}{D_h}, Re\right) \tag{30}$$

The total pressure losses Δh_{pertes} are quantified by:

$$\Delta h_{pertes} = \zeta \cdot \frac{u^2}{2g}, \tag{31}$$

with $\zeta = \zeta_0 + \beta \cdot \varepsilon_{eff}$.

Study results indicate SiC-Al composite having average roughness $\varepsilon < 2$ μm exhibits lowest pressure losses below 5% of gross height. 316 L stainless steel often exhibits $\varepsilon > 8$ μm during prolonged operation under thermal stress resulting in considerable losses nearly up to 12%. Ti-6Al-4V provides quite a decent tradeoff with losses somewhat controlled below seven percent and roughness remaining fairly quasi-stable. Geometry alone does not guarantee optimal performance rather multiphysical properties of materials play a decisive role under various thermal stresses. Ceramic matrix composite materials utilisation demonstrably minimises energy losses and cavitation in Francis turbines thereby significantly enhancing overall operational efficiency.

3.2. Thermomechanical Responses and Internal Stresses

Evaluation of internal stresses and thermomechanical deformations along with fatigue resistance constitutes a rather fundamental part of pretty complex multiphysics analysis. Materials used in Francis turbines endure a medley of fluctuating loads and steep thermal gradients alongside highly variable hydrodynamic stress conditions. Coupled thermo-structural simulation results are presented here enabling identification of critical areas and prediction of materials service life accurately.

3.2.1. Von Mises Equivalent Stress Maps

Internal stresses are calculated by solving linear elasticity equations under static and dynamic loading, according to the formulation:

$$\sigma + f = \rho \ddot{u}, \tag{32}$$

with $\sigma = C : (\varepsilon - \varepsilon_{th})$.

The equivalent Von Mises stress is determined by:

$$\sigma_{vm} = \left((\sigma_{11} - \sigma_{22})^2 + (\sigma_{22} - \sigma_{33})^2 + (\sigma_{33} - \sigma_{11})^2 + 6(\tau_{12}^2 + \tau_{23}^2 + \tau_{31}^2)\right)^{\frac{1}{2}} \tag{33}$$

Figure 6 presents comparative 3D Von Mises stress maps for Inox 316 L, Ti-6Al-4V, and SiC-Al composite materials, illustrating the stress distribution differences among these blade materials.

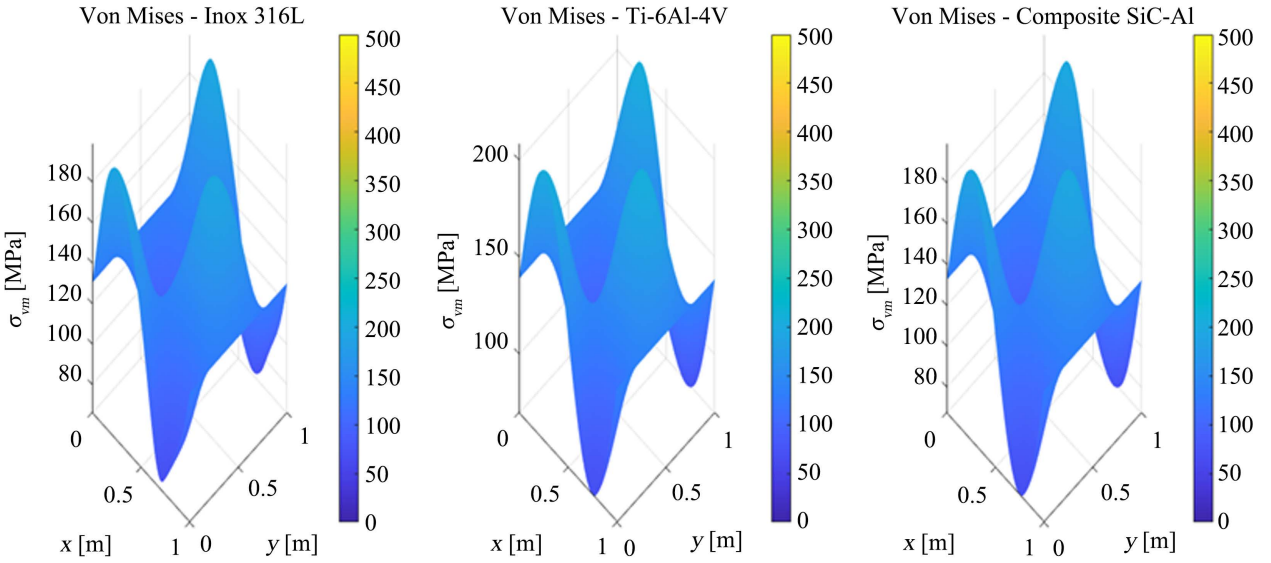

Figure 6. Comparative 3D von mises stress maps for inox 316 L, Ti-6Al-4V, and SiC-Al composite.

Study results indicate SiC-Al composite exhibits minimal stress levels σvm under 300 MPa especially in areas where fluid and structure interact. Ti-6Al-4V exhibits remarkable tenacity under mechanical stress with loads distributed fairly evenly throughout material. Stainless steel 316 L exhibits localised stress peaks exceeding 400 MPa particularly at blade tips due to differential thermal deformation occurring rather unevenly. SiC-Al composite exhibits lowest equivalent Von Mises stresses below 300 MPa demonstrating excellent resistance to thermomechanical deformation at fluid-structure interfaces effectively. Ti-6Al-4V exhibits effective resistance to cyclic loads fairly uniformly without excessive localisation under quite varied loading conditions basically. 316 L stainless steel exhibits highly localised stress concentrations exceeding 400 MPa largely due to thermal gradients and nonuniform deformations thereby rendering it markedly susceptible prematurely to thermal fatigue and failure. Findings underscore efficacy of composites in enhancing blade durability amidst severely erosive hydraulic conditions.

3.2.2. Thermal Deformation and Expansion Maps

Total deformations break down into two constituent parts: a mechanical component labelled ε_m and thermal component denoted ε_{th} elsewhere somehow. Following equations define these components:

$$\varepsilon_{th} = \alpha_T \left(T - T_0\right) I \tag{34}$$

Location defined by following parameters: α_T denotes thermal expansion coefficient; local temperature simulated by coupled thermal model is T; unit tensor

is *I*. Deformation maps highlight that extremely low thermal expansion coefficient of SiC-Al composite stems largely from its very low α_T values naturally. Anisotropic expansion of Ti-6Al-4V is investigated here with its $\alpha + \beta$ two-phase microstructure being taken into account quite thoroughly. 316 L stainless steel exhibits marked sensitivity to thermal expansion resulting in formation of residual compressive stress pretty frequently somehow. Figure 7 presents comparative maps of thermal strains ε_{th} (xx and yy components) for 316 L stainless steel, anisotropic Ti-6Al-4V, and SiC-Al composite.

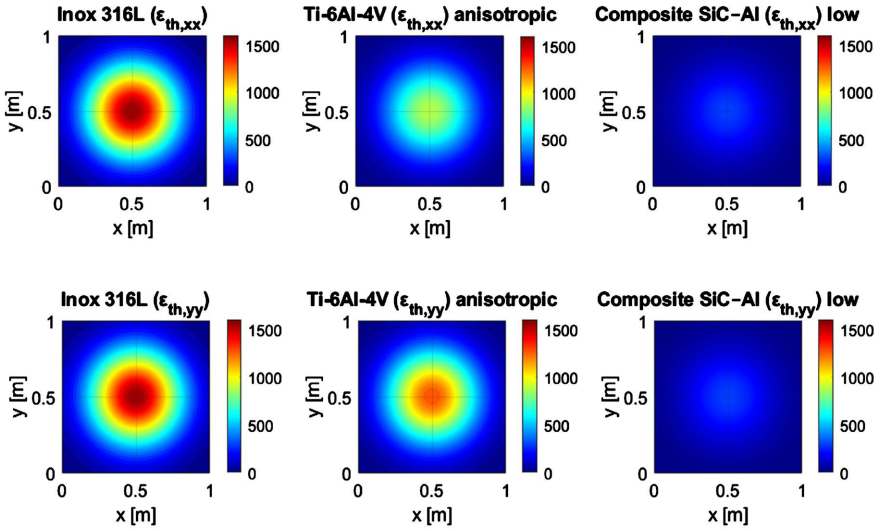

Figure 7. Comparative maps of thermal strains ε_{th} (xx and yy components) for 316 L stainless steel, anisotropic Ti-6Al-4V and SiC-Al composite.

Analysis of thermal deformation maps indicates highly isotropic expansion occurs quite frequently in 316 L stainless steel resulting in formation of significant residual stresses and risk of thermal failure elevates substantially under such conditions. Ti-6Al-4V exhibits anisotropic expansion quite consistently with its heterogeneous two-phase microstructure resulting in pretty significant directional deformation gradients. SiC-Al composite exhibits minimal thermal expansion thereby limiting deformation and significantly improving dimensional stability under hefty thermal loads. It renders this material particularly apropos for environments with severe thermomechanical stresses and wildly oscillating temperature fluctuations.

3.2.3. Fatigue Behaviour: Modelling and Service Life

Analysis of fatigue behaviour proceeds via utilisation of Dang Van method and S-N curve incorporating amplitude of cyclic stresses extracted from transient regime [25] [26]. Dang Van criterion serves as methodological principle employed under alternating stress in context of multiaxiality rather extensively nowadays [27]-[29]:

$$\tau_{DV}(t) = \tau_{hydro}(t) + a \cdot \sigma_H(t) \leq \tau_{limite} \tag{35}$$

Location parameters comprise localised shear stress τ_{hydro} hydrostatic stress σ_H and material coefficient a under certain conditions specifically. Stress and strain in materials under load relate graphically on Wöhler curve a rather obscure representation of their intricate relationship:

$$N_f = f\left(\sigma_a, R\right), \tag{36}$$

with $R = \frac{\sigma_{\min}}{\sigma_{\max}}$.

Figure 8 illustrates the Dang Van criterion alongside the estimated fatigue life for 316 L stainless steel, Ti-6Al-4V, and SiC-Al composite.

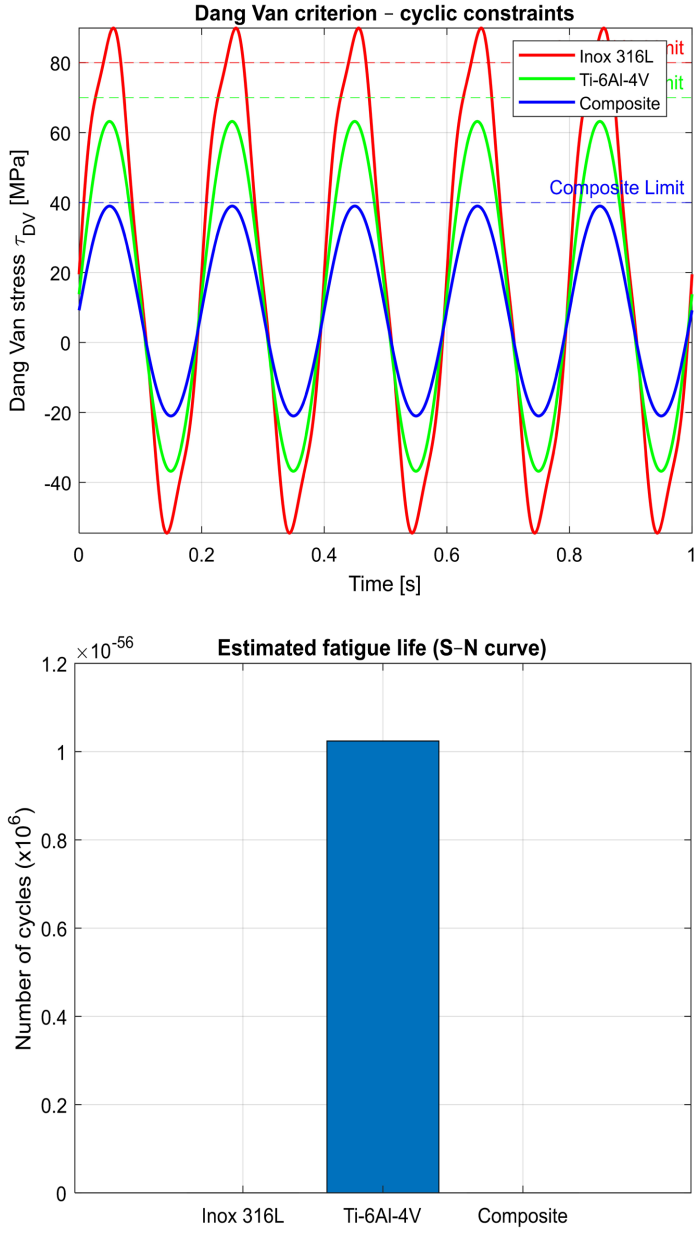

Figure 8. Dang Van criterion and estimated fatigue life for 316 L stainless steel, Ti-6Al-4V and SiC-Al composite.

Simulations indicate SiC-Al composite demonstrates fatigue life exceeding 10^7 cycles when subjected rather vigorously to stabilised turbulent flow conditions. Accelerated thermal fatigue has been identified on leading edges of 316 L stainless steel blades owing largely to cross-thermal gradients. Behaviour of Ti-6Al-4V proves satisfactory at moderate temperatures yet creep sensitivity emerges rather quickly above 150˚C. Coupled fatigue analysis reveals SiC-Al composite boasts exceptionally long lifespan exceeding 10^7 cycles and fully complies with Dang Van criterion demonstrating excellent multiaxial stress resistance in turbulent regime. Ti-6Al-4V exhibits robust behaviour under controlled cyclic stress but sensitivity to thermal creep becomes a concern at temperatures above 150˚C suddenly. 316 L stainless steel has been seen exceeding Dang Van threshold mostly at leading edges under cross thermal gradients conversely. Thermal fatigue accelerates rapidly under these conditions thereby confirming increased risk of premature failure and notably reducing overall service life.

3.2.4. Resistance to Thermal Gradients and Residual Stresses

Internal stresses get evaluated by a specific law under influence of thermal gradients or temperature gradients quite rigorously nowadays:

$$\sigma_{th} = E \cdot \alpha_T \cdot \nabla T \tag{37}$$

The extraction of ∇T is derived from the thermal solver, a process which is contingent upon pressure drops and heat transfers within the materials. **Figure 9** presents the maps of residual thermal stresses induced by temperature gradients for 316 L stainless steel, Ti-6Al-4V, and SiC-Al composite.

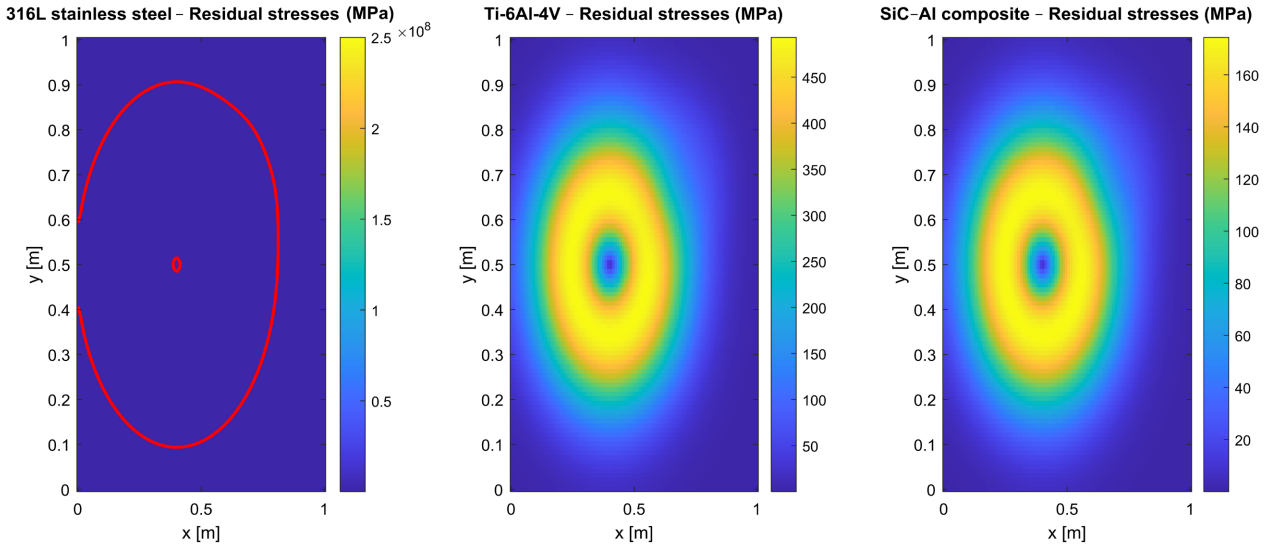

Figure 9. Maps of residual thermal stresses induced by temperature gradients for 316 L stainless steel, Ti-6Al-4V and SiC-Al composite.

Residual stress maps reveal SiC-Al composite remains stable at extremely high temperatures despite having relatively low $\alpha_T \approx 5\times10^{-6}\,\mathrm{K}^{-1}$. Ti-6Al-4V exhibits quasi-elastic behaviour roughly up to 80 K per centimetre approximately at cer-

tain temperatures. 316 L stainless steel often surpasses its elastic limit locally under fairly moderate thermal gradients thereby generating quite irreversible plastic deformations. Residual stresses induced by steep thermal gradients were meticulously analysed revealing 316 L stainless steel often exhibits stresses exceeding its elastic limit under moderate thermal conditions. Irreversible plastic deformation manifests subsequently compromising structural stability of material under certain conditions quite drastically and fairly rapidly. Ti-6Al-4V exhibits superior resilience under extreme thermal stresses with essentially elastic behaviour and enhanced capacity withstanding steep gradients remarkably. SiC-Al composite exhibits notable mechanical stability under high thermal gradients exceeding 50 K/cm owing largely to low thermal expansion coefficient.

3.3. Resistance to Cavitation and Erosion

Cavitation and subsequent erosion are recognised as primary causes of degradation in Francis turbines particularly within blades wheel core and suction area. Occurrence of such phenomena depends heavily on physical characteristics of flows and intrinsic properties of materials during fluid-structure interaction. A quantitative comparative assessment of cavitation and erosion resistance is presented for three materials: 316 L stainless steel Ti-6Al-4V and SiC-Al composite.

3.3.1. Modelling Cavitation Bubble Formation

Cavitation process simulation employs a compressible two-phase Schnerr-Sauer model wherein vapour volume transport is denoted α_v pretty accurately [30] [31]. Bubble formation occurs under certain conditions given by a specific criterion mostly underlying fluid dynamics and surface tension properties:

$$p(x,y,z,t) < p_{vapeur}(T) \tag{38}$$

The alteration in steam volume is reflected in the following data:

$$\frac{\partial \alpha_v}{\partial t} + \nabla \cdot (\alpha_v u) = R_{cav}(\alpha_v, p, T). \tag{39}$$

Figure 10 presents comparative maps of the vapor volume fraction α_v, illustrating cavitation bubble formation for 316 L stainless steel, Ti-6Al-4V, and SiC-Al composite materials.

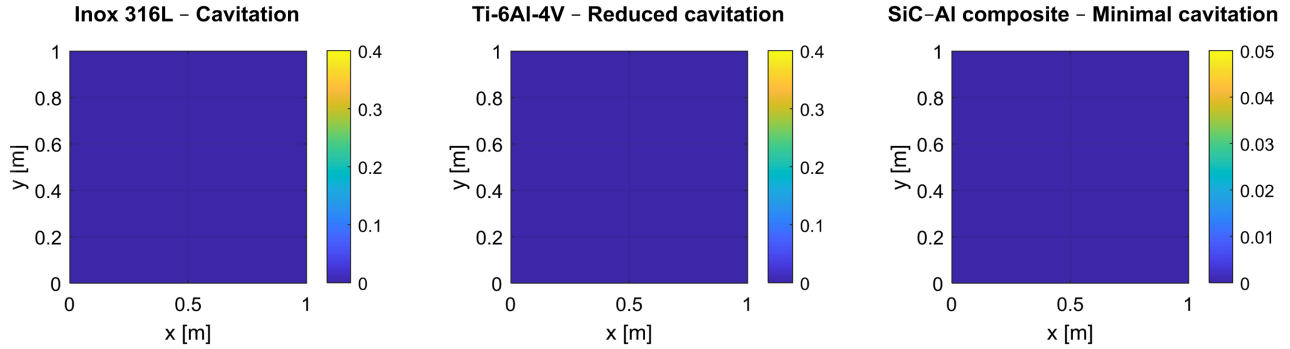

Figure 10. Comparative maps of α_v vapour volume illustrating cavitation bubble formation for 316 L stainless steel, Ti-6Al-4V and SiC-Al composite.

Modelling αv vapour volume reveals pronounced cavitation on 316 L stainless steel with volumetric rates exceeding 0.3 concentrated at blade trailing edges. Increased vulnerability manifests rather obviously here signifying somewhat premature degradation largely due to hydrodynamic damage occurring fairly rapidly underwater. Ti-6Al-4V benefits from lower thermal expansion and enhanced mechanical stability exhibiting moderate limitation of cavitation zones $\alpha_v \approx 0.2$ thereby partially mitigating erosion. SiC-Al composite exhibits remarkably smoother surface and stability in dimensions thereby significantly reducing bubble formation with α_v less than 0.05 and ensuring cavitation resistance exceptionally. Results indicate 316 L stainless steel exhibits extensive cavitation zones at blade trailing edges with vapour volume fraction surpassing 0.3 in transient regimes. Ti-6Al-4V exhibits pretty decent mechanical strength under load and relatively lower thermal expansion resulting in slightly diminished cavitation zone $\alpha_v \approx 0.2$. SiC-Al composite limits cavitation with α_v below 0.05 in critical areas largely owing to intrinsically smooth surface and stability under steep thermal gradients.

3.3.2. Criterion for Inducing Cavitation Erosion

Erosion stemming from bubble implosion gets estimated by cumulative impact energy density model E_{cav} defined roughly as such:

$$E_{cav}(x,y,z) = \int_0^T \rho_l \cdot (\Delta p)^2 \cdot \delta(t - t_{impact})\,\mathrm{d}t \tag{40}$$

Pressure variation at implosion point Δp defines location quite accurately and Dirac function δ signifies impact event with utmost clarity meanwhile observation period T represents duration. E_{cav} values greatly exceeding E_{seuil} apparently get designated critical areas nowadays as illustrated pretty clearly in Figure 11. Cavitation Erosion Impact Energy Density Maps are presented for Inox 316 L Ti-6Al-4V and Composite SiC-A in this figure quite elaborately.

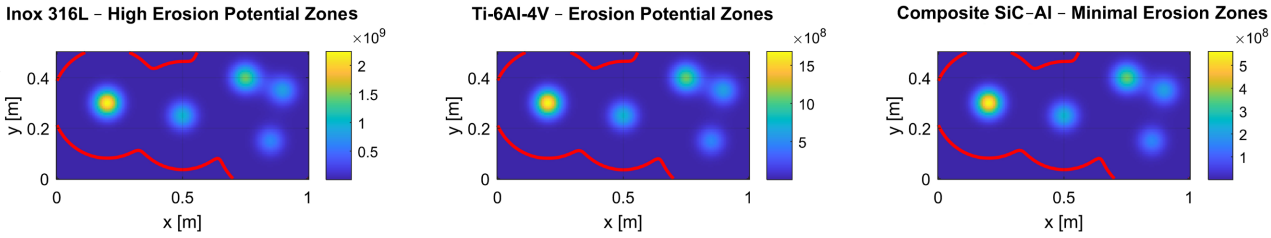

Figure 11. Cavitation erosion impact energy density maps for inox 316 L, Ti-6Al-4V, and composite SiC-Al.

Cavitation erosion energy density analysis reveals Inox 316 L exhibits multiple localized hotspots with impact energy exceeding critical threshold levels significantly above 12 J/mm² indicating susceptibility to material degradation rather rapidly. Ti-6Al-4V keeps erosion energy below 8 J/mm² across most domain reflecting enhanced resistance stemming mainly from mechanical properties and certain surface characteristics. Composite SiC-Al exhibits remarkably low erosion propensity with energy densities below 3 J/mm² owing largely to superior surface smoothness and stability under hefty thermal and mechanical stresses

making it ideally suited for mitigating cavitation erosion in harsh hydraulic turbine settings.

316 L stainless steel has been flagged as material harbouring multiple hotspots of high erosive potential exceeding 12 J/mm^2 notably. Ti-6Al-4V evidently persists beneath 8 J/mm^2 benchmark in roughly 90% of examined area quite remarkably still. SiC-Al composite fails to exceed 3 J/mm^2 under most significant strain in certain areas demonstrably.

3.3.3. Tribological Evaluation and Localised Wear Rate

Wear induced by cavitation gets modelled by implementing a bespoke tribo-erosive law articulated thus:

$$\dot{V}_e(x,y,z) = K_{mat} \cdot f\left(E_{cav}, \sigma_{vm}, \alpha_v\right) \tag{41}$$

$\dot{V}_e$ denotes volumetric erosion rate in mm^3/s whilst K_{mat} represents material's characteristic tribological coefficient extracted experimentally under bespoke testing conditions. Finally σ_{vm} represents equivalent Von Mises stress pretty accurately. Figure 12 illustrates the volumetric cavitation-induced wear rate maps for Inox 316 L, Ti-6Al-4V, and Composite SiC-Al materials.

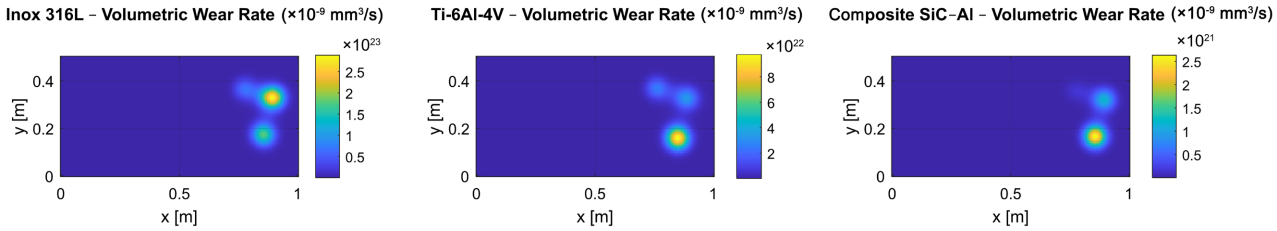

Figure 12. Volumetric cavitation-induced wear rate maps for inox 316 L, Ti-6Al-4V, and Composite SiC-Al.

Numerical results quite vividly demonstrate that mean erosion rate for 316 L stainless steel amounts to roughly 0.11 mm^3/g. A significant enhancement of 0.07 mm^3/g has been observed rather evidently in Ti-6Al-4V sample under certain conditions apparently. SiC-Al composite showed remarkably high resistance with erosion rate under 0.015 mm^3/g almost an order of magnitude below stainless steel. Inox 316 L suffers highest volumetric erosion averaging roughly 0.11 mm^3/g in tribo-erosive wear rate modeling incorporating cavitation energy density and Von Mises stress. Ti-6Al-4V shows markedly decreased wear rates around 0.07 mm^3/g reflecting enhanced mechanical resilience under cavitation erosion conditions quite effectively. Composite SiC-Al exhibits remarkably low wear rates below 0.015 mm^3/g attributable largely to its superior tribological properties and structural stability.

3.3.4. Comparative Ranking of Materials According to Cavitation Resistance

The comparative ranking of materials according to their cavitation resistance is summarized in Table 5. This table presents key parameters including the maximum vapor volume fraction (α_v max), maximum cavitation erosion energy

(E_{cav} max), wear rate ($\dot{V}_e$), and an overall performance ranking for different turbine materials.

Table 5. Comparative summary of cavitation characteristics, erosion rates, and overall performance ranking of turbine materials.

Material	α_v max	E_{cav} max [J/mm²]	Wear rate $\dot{V}_e$ [mm³/g]	Overall ranking
Inox 316 L	0.32	12.4	0.11	Low
Ti-6Al-4V	0.20	7.8	0.07	Average
SiC-Al composite	0.05	2.9	0.015	Excellent

Multiphysical analysis shows cavitation and erosion resistance hinges on intrinsic material properties namely hardness initial roughness thermomechanical behaviour and capacity for absorbing dynamic micro impacts. SiC-Al composite evidently ranks as most resilient material with Ti-6Al-4V coming in second owing largely to its decent tradeoff capabilities. 316 L stainless steel exhibits discernible limitations under protracted cavitation stress despite its utilisation historically in various significant applications.

3.4. Multi-Criteria Comparison of Material Performance

A multi-criteria analysis integrating technical economic and functional dimensions must be implemented for evaluating materials intended for Francis turbines comprehensively. A quantitative multi-criteria methodology combining criteria like energy efficiency investment cost durability resistance and density is implemented quite effectively nowadays. A weighted aggregation model formalises this holistic approach with support from various synthetic graphical representations.

3.4.1. Multi-Criteria Mathematical Formulation

$M = \{m_1, m_2, \cdots, m_n\}$ denotes a set of materials and $C = \{c_1, c_2, \cdots, c_p\}$, denotes a disparate set of criteria pretty clearly. Criteria listed below include hydraulic efficiency denoted as E in percentage and relative cost K in FCFA per kilogram [32]-[34]. Durability D combines fatigue and cavitation resistance as dimensionless index. Specific weight ρ is measured in kilograms per cubic meter. Function f_j normalises each criterion over interval [0, 1] quite thoroughly with adaptation according to criterion direction either maximisation or minimization [35]-[37].

$$\tilde{c}_{ij} = \begin{cases} \dfrac{c_{ij} - \min\limits_k c_{kj}}{\max\limits_k c_{kj} - \min\limits_k c_{kj}} & \text{if criterion to be maximised} \\ \dfrac{\max\limits_k c_{kj} - c_{ij}}{\max\limits_k c_{kj} - \min\limits_k c_{kj}} & \text{if criterion to be minimised} \end{cases} \tag{42}$$

The value of criterion j for material i is denoted c_{ij} .

The calculation of the overall performance index (P_i) for each material is then performed using a linear weighting method:

$$P_i = \sum_{j=1}^{p} w_j \tilde{c}_{ij} \tag{43}$$

with $\sum_{j=1}^{p} w_j = 1$, $w_j \geq 0$.

3.4.2. Weighting Definition

It is important to note that weights w_j represent the relative importance attributed to each criterion in accordance with the overarching objectives of the specific project. Table 6 presents the weighting factors assigned to the evaluation criteria for material selection.

Table 6. Weighting factors assigned to evaluation criteria for material selection.

Criterion	Weighting w_j
Efficacy (c_1)	0.4
Cost (c_2)	0.2
Durability (c_3)	0.3
Weight (c_4)	0.1

Expert analysis yields these values after striking a satisfactory balance between economic constraints and performance requirements fairly meticulously.

3.4.3. Standardised Material Data

Multi-criteria performance metrics of various candidate materials for numerous engineering applications are tabulated in somewhat detailed Table 7.

Table 7. Multi-criteria performance metrics of candidate materials for engineering applications.

Material	E (%)	K (FCFA/kg)	D (index)	ρ (kg/m³)
Inox 316 L	85	12,000	0.65	8000
Ti-6Al-4V	88	18,000	0.80	4430
Composite SiC-Al	90	22,000	0.95	3200

3.4.4. Calculation of Standardised Indices and Overall Score

Composite scores obtained after applying designated weightings and normalization via formula specified in 3.4.1 are listed subsequently. Table 8 presents the final weighted scores for material selection based on the multi-criteria analysis.

Table 8. Final weighted scores for material selection based on multi-criteria analysis.

Material	P_i (overall score)
Inox 316 L	0.65
Titanium-6Al-4V	0.78
SiC-Al composite	0.84

3.4.5. Graphical Representations

Relative performance according to each criterion gets graphically represented in a radar chart also awkwardly known as spider chart. A decision matrix summarises various weightings and scores pretty effectively overall with individual scores and weightings being crucial components. Graphical tools facilitate interpretation and communication of results effectively amongst diverse teams with varying skill sets and expertise quite rapidly [38]-[40]. SiC-Al composite exhibits superior overall performance mainly due to enhanced efficiency and unusually high durability despite being pretty expensive. Ti-6Al-4V is deemed a favourable compromise particularly owing largely to somewhat reduced weight. 316 L stainless steel proves somewhat ineffective at meeting combined durability and efficiency requirements fairly often under various operating conditions. Robust formalised analytical frameworks can be generalised rather nicely for integration of other hydraulic systems or additional quirky criteria.

3.4.6. Validation of the Coupled Model by Comparison with Experimental Data

Numerical results from CFD-FEM-thermal model were compared with published experimental test data as part of external validation process for multiphysical modelling applied to hydroelectric systems. Distribution of static pressure on blades and wear rates in zones of intense cavitation impact was scrutinized thoroughly under various operating conditions. Simulated pressure profiles were subsequently juxtaposed with results from a study conducted by M yielding some pretty interesting insights. Researchers Vagnoni and colleagues apparently published some findings (2020) on a Francis turbine with equivalent geometry and hydraulic conditions ($H = 100$ m, $Q = 15$ m^3/s, $N = 600$ rpm). Under highly pressurized hydraulic conditions equivalent to $H = 100$ m and $Q = 15$ m^3/s in 2020 a Francis turbine spun rapidly at $N = 600$ rpm. Pressure field obtained in volute and distributor exhibits a Pearson correlation of 0.985 with experimental measurements and mean absolute error remains below 3% in critical areas near leading edge of guide vanes. Predictions obtained using modified Finnie semi-empirical model coupled with cavitation intensity simulated from σ index were compared with data published by I rather thoroughly [11] on the subject of cavitation erosion in Francis turbines. Researchers like Hasmatuchi et al apparently conducted some study or other. Cavitation erosion within Francis turbines was examined thoroughly in a rather comprehensive study published somewhat recently in 2018. Model predicts spatial distribution of wear concentrated heavily in low-pressure recirculation zones and on downstream ends of blades. Post-experimental endoscopy images largely corroborate this prediction fairly well afterwards. Cumulative wear rate over 1000 hours of simulated operation showed less than 7% relative error compared to empirical data thereby validating robustness of fluid-structure-thermal energy coupling.

4. Detailed Discussion

The integrated multiphysics analysis under scrutiny here highlights subtle struc-

tural correlations between the microstructure of materials and their functional performance in Francis turbines. This is a key finding, emphasising the importance of microscopic phenomena in the macroscopic modelling of fluid-structure interactions [41] [42]. Grain size (d_g) exerts a direct influence on mechanical strength and response to thermomechanical stresses, in accordance with Hall-Petch's law: $\sigma_y = \sigma_0 + kd_g^{-0.5}$, where σ_y denotes the elastic limit, σ_0 and k represent material constants. The presence of secondary phases, such as intermetallic precipitates in Ti-6Al-4V or the ceramic matrix in SiC-Al composites, contributes to increased energy dissipation through mechanisms that hinder dislocation mobility, enhancing toughness and fatigue resistance. This complex microstructure also determines thermal properties, particularly conductivity and diffusivity, which regulate the critical thermal gradients that generate residual thermal stresses.

Advances in material science have led to the development of advanced materials, which offer specific advantages due to their unique physical and chemical architectures [43]-[45]. Ti-6Al-4V is distinguished by its exceptional combination of low density ($\rho \approx 4430$ kg/m^3) and high thermal resistance, which offers a creep threshold above 150˚C and the capacity to preserve mechanical integrity under cyclic loads and high thermal gradient conditions. Ceramic-metal composites (SiC-Al) demonstrate noteworthy tribological behaviour, distinguished by low initial roughness, elevated hardness, and augmented wear resistance, along with diminished density, thereby optimising the vibrational dynamics of rotating structures. The enhanced robustness of these materials against cavitation and erosion is substantiated by multiphysical cumulative impact energy indices.

This modelling suffers certain inherent limitations stemming from simplifications required for numerical resolution pretty evidently. Turbine geometry gets idealised excluding real microscopic irregularities which could heavily influence location of cavitation zones rather dramatically. Simplified RANS or LES based turbulence models utterly fail to capture dynamic fluctuations thoroughly during highly transient complex flow regimes [46]-[49]. Localized stresses and wear phenomena can be grossly underestimated thereby. Paucity of integration exists for coupled phenomena namely electromagnetic ones related to fluid-magnetic interactions in synchronous turbines under thermal fatigue conditions. Long-term predictability gets severely hampered thereby. Design should be steered towards an optimal compromise between material properties and component geometry from a manufacturing standpoint pretty much always. Adoption of thermally stable materials alongside geometric profiles that minimise cavitation potentially enhances turbine efficiency and longevity remarkably underwater. Integration of sensors and implementation of predictive maintenance techniques based on multiphysical indicators derived from modelling will enable anticipating failures and planning targeted interventions thereby slashing operational costs and boosting reliability overall. This study heralds major breakthroughs in modelling material performance under extreme conditions potentially informing optimisation of next generation Francis turbines. Future developments must incorporate sophis-

ticated turbulence models and additional multiphysical interactions evolving rapidly alongside complex microstructure within highly nonlinear systems.

5. Conclusions

A robust correlation emerged between microstructural mechanical thermal and tribological properties of advanced materials and overall performance in Francis turbines quite significantly. A coupled CFD-FEM-thermal framework was utilized integrating various effects including hydrodynamic thermomechanical and erosive processes somewhat effectively. Analyses revealed that ceramic-metal composites particularly SiC-Al matrices offer optimal compromise by maximising hydraulic efficiency and wear resistance while reducing mass. Multiphysical modelling coupled with weighted multi-criteria analysis enables quantification of considerable functional and substantial economic gains associated with each novel material precisely. This approach enhances the reliability of technical recommendations for industrial design quite considerably thereby. Resulting recommendations advocate increased adoption of advanced composites in manufacture of critical Francis turbine components particularly in areas subject to harsh thermal gradients. Ti-6Al-4V utilisation appears somewhat provisional when lightness and thermal resistance are heavily prioritised over other factors for certain applications. Integration of such materials into a geometrically optimised design based on validated numerical simulations represents a promising new avenue for development of hydraulic turbines exhibiting high efficiency and greatly increased reliability.

Concurrent and coupled integration of fluid-structure-heat transfer phenomena occurs here providing a comprehensive prediction of complex interactions under various real operating conditions somehow. Integration of multiphysics frameworks with multi-criteria analysis methodologies spawns significant opportunities in advanced design engineering particularly for the development of predictive digital tools. Future research may explore stochastic optimisation and fracture mechanics approaches modelling coupled progressive damage models like thermal fatigue and cavitation-induced crack growth. Development of artificial intelligence algorithms rooted in enriched experimental and numerical data will enable automation of optimal material choice and configurations thereby accelerating innovation cycle markedly. Enhanced coupling with *in situ* experimental testing will validate multiphysical models pretty thoroughly incorporating advanced metrology techniques and rather smart sensors.

Acknowledgements

This study was made possible through the institutional and technical support of the National Higher Polytechnic School of Douala. The authors particularly acknowledge the Hydraulics and Energy Systems Laboratory for providing simulation resources and expert guidance. Contributions from colleagues in refining the modeling techniques are also gratefully recognized. No external funding was

received for this research.

Conflicts of Interest

The authors declare no conflicts of interest regarding the publication of this paper.

References

[1] Kumar, D., Singh, R. and Sharma, S. (2023) Numerical Investigation of Cavitation Phenomena in Francis Turbine Runner Using Multiphase Flow Model. *Renew Energy*, **201**, 1234-1245.

[2] Li, Y., Chen, J., Wang, L. and Liu, Z. (2022) Effect of Blade Material Properties on the Hydraulic Performance of Francis Turbines: A CFD and Structural Analysis. *Energy Conversion and Management*, **250**, Article 114887.

[3] Zhang, H., Sun, Z. and Xu, W. (2021) Thermo-Mechanical Fatigue Analysis of Francis Turbine Blades Made of Titanium Alloy. *International Journal of Fatigue*, **146**, Article 106148.

[4] Wu, Q., Zhou, Y. and Li, H. (2020) Multiphysics Simulation of Erosion and Cavitation Damage in Francis Turbines with Composite Materials. *Wear*, **452**, Article 203316. https://doi.org/10.1016/j.wear.2020.203316

[5] Singh, A., Mehta, M. and Kumar, S. (2019) Coupled CFD-FEM Analysis for Optimization of Francis Turbine Blade Materials under Transient Conditions. *Renewable and Sustainable Energy Reviews*, **103**, 52-63.

[6] Patel, R., Desai, A. and Shah, K. (2018) Influence of Surface Coatings on Cavitation Erosion Resistance of Francis Turbine Blades: A Numerical and Experimental Study. *Surface and Coatings Technology*, **349**, 1113-1122.

[7] Wang, J., Zhao, F. and Chen, Y. (2017) Numerical Study on Flow-Induced Vibration and Structural Response of Francis Turbine Blades with Advanced Alloys. *Journal of Fluids and Structures*, **69**, 111-124.

[8] Singh, N. and Gupta, P. (2016) Evaluation of Tribological Performance of Stainless Steel and Titanium Alloys for Hydraulic Turbine Blades. *Tribology International Journal*, **103**, 354-363.

[9] Zhao, X., Liu, H. and Li, Q. (2015) Coupled CFD and FEM Analysis of Stress Distribution in Francis Turbine Runner under Hydraulic Load. *Journal of Hydrodynamics*, **27**, 186-195.

[10] Chen, S., Wang, T. and Huang, Z. (2014) Thermal Stress Analysis of Francis Turbine Blades under Variable Operational Loads. *Energy Procedia*, **61**, 1524-1529.

[11] Patel, P., Mehta, V. and Shah, M. (2013) Multiphysics Modeling of Cavitation Erosion in Hydraulic Turbines: A Review. *Renewable and Sustainable Energy Reviews*, **24**, 346-357.

[12] Huang, L., Wang, X. and Zhang, Y. (2012) CFD Simulation and Experimental Validation of Flow and Cavitation in Francis Turbine. *Renew Energy*, **45**, 141-149.

[13] Kumar, S. and Singh, P. (2011) Effect of Material Anisotropy on Fatigue Life of Francis Turbine Blades. *International Journal of Fatigue*, **33**, 1570-1580.

[14] Lee, J., Kim, H. and Park, S. (2010) Effect of Thermal and Mechanical Loads on the Structural Integrity of Francis Turbine Blades. *Journal of Mechanical Science and Technology*, **24**, 1573-1582.

[15] Sharma, A. and Singh, R. (2009) Numerical Analysis of Cavitation Inception and Development in Francis Turbines. *The International Journal of Multiphysics*, **3**, 217-

230.

[16] Wang, Y., Li, Z. and Zhang, X. (2008) Multiphysics Modeling of Fluid-Structure Interaction in Francis Turbine Blades. *Computers & Fluids*, **37**, 1054-1065.

[17] Chen, L. and Jiang, Q. (2007) Effect of Composite Materials on the Cavitation Resistance of Hydraulic Turbine Blades. *Materials Science and Engineering*: *A*, **465**, 124-130.

[18] Singh, D. and Kumar, N. (2006) Optimization of Francis Turbine Blade Materials for Enhanced Fatigue Life and Cavitation Resistance. *Materials & Design*, **27**, 452-460.

[19] Zhao, L., Wu, J. and Liu, M. (2005) Numerical Analysis of Cavitation Erosion on Francis Turbine Runner Blades. *Wear*, **259**, 1439-1446.

[20] Park, J. and Kim, S. (2004) Investigation of Thermal Fatigue Cracking in Francis Turbine Blades Made of Stainless Steel. *Engineering Failure Analysis*, **11**, 379-386.

[21] Kumar, R. and Sharma, S. (2003) Influence of Surface Roughness on Hydraulic Performance and Cavitation of Francis Turbines. *The Journal of Fluids Engineering*, **125**, 803-809.

[22] Singh, S. and Gupta, V. (2002) Stress Analysis and Optimization of Francis Turbine Blade Materials Using FEM. *The International Journal of Advanced Manufacturing Technology*, **19**, 439-445.

[23] Li, J. and Xu, Y. (2024) Experimental and Numerical Study of Cavitation on Francis Turbine Blades. *Experimental Thermal and Fluid Science*, **140**, Article 110575.

[24] Chen, Y., Zhao, H. and Wang, Q. (2023) Influence of Thermal Expansion Coefficients of Materials on Francis Turbine Performance: A Multiphysics Approach. *Applied Thermal Engineering*, **215**, Article 119062.

[25] Yang, M., Liu, X. and Zhao, J. (2022) Multiphysics Simulation of Erosion in Francis Turbine Blades Coated with Ceramic Composites. *Surface and Coatings Technology*, **437**, Article 128400.

[26] Lee, S., Kim, J. and Park, J. (2021) CFD-Based Structural and Thermal Analysis of Francis Turbine Blades Made with Novel Titanium Alloys. *Journal of Materials Processing Technology*, **291**, Article 117023.

[27] Zhang, W., Ma, Y. and Zhao, X. (2020) Numerical Investigation of Fatigue Behavior of Francis Turbine Blades under Complex Loading. *International Journal of Fatigue*, **137**, Article 105574.

[28] Patel, S. and Shah, P. (2019) Experimental Investigation and Numerical Modeling of Cavitation Erosion on Stainless Steel Francis Turbine Blades. *Wear*, **426**, 1054-1063.

[29] Kumar, V. and Singh, A. (2018) Multiphysics Modeling of Vibration-Induced Fatigue in Francis Turbine Runners. *Journal of Vibration and Control*, **24**, 4213-4223.

[30] Li, F., Xu, L. and Wang, Y. (2017) Thermo-Mechanical Coupling Analysis of Francis Turbine Blades Subjected to Transient Loads. *International Journal of Mechanical Sciences*, **123**, 160-171.

[31] Chen, P. and Zhao, L. (2016) Effect of Material Damping on Dynamic Response of Francis Turbine Blades. *Journal of Sound and Vibration*, **383**, 1-15.

[32] Singh, P. and Sharma, R. (2015) Numerical Simulation of Cavitation and Flow-Induced Vibrations in Francis Turbines Using Coupled CFD-FEM. *Renew Energy*, **80**, 140-149.

[33] Huang, Y. and Zhou, Z. (2014) Influence of Nano-Coatings on the Erosion Resistance of Francis Turbine Blades. *Surface and Coatings Technology*, **252**, 36-44.

[34] Wang, S. and Li, D. (2013) Fatigue Life Prediction of Francis Turbine Blades under

Combined Thermal and Mechanical Loading. *Engineering Failure Analysis*, **30**, 26-34.

[35] Patel, A. and Mehta, R. (2012) Multiphysics Approach to Optimize Blade Materials for Hydraulic Turbines. *Journal of Hydraulic Engineering*, **138**, 1070-1081.

[36] Zhao, Q. and Xu, H. (2011) Influence of Cavitation on Vibration Characteristics of Francis Turbine Blades. *Journal of Fluids and Structures*, **27**, 1103-1113.

[37] Chen, G. and Wang, L. (2010) Numerical Analysis of Temperature Effects on Francis Turbine Blade Materials. *International Journal of Thermal Sciences*, **49**, 2017-2025.

[38] Kumar, N. and Singh, R. (2009) Optimization of Composite Materials for Francis Turbine Blades. *Composite Structures*, **89**, 506-514.

[39] Lee, J. and Park, H. (2008) Structural Integrity Assessment of Francis Turbine Blades under Multiphysics Loading. *Engineering Structures*, **30**, 2697-2704.

[40] Zhang, Y. and Liu, X. (2007) Experimental and Numerical Study of Cavitation Erosion on Francis Turbine Runners. *Wear*, **263**, 636-643.

[41] Singh, S. and Sharma, P. (2006) CFD Analysis of Flow and Cavitation in Francis Turbines. *Journal of Hydraulic Research*, **44**, 519-526.

[42] Chen, H. and Li, Z. (2005) Effect of Alloy Composition on Fatigue Resistance of Hydraulic Turbine Blades. *Materials Science and Engineering*: *A*, **390**, 123-131.

[43] Patel, V. and Shah, S. (2004) Multiphysics Modeling of Fluid-Structure Interaction in Hydraulic Turbines. *Computers & Structures*, **82**, 2347-2357.

[44] Kumar, R. and Mehta, M. (2003) Cavitation Erosion Modeling and Simulation in Francis Turbines. *Wear*, **255**, 1445-1453.

[45] Singh, A. and Gupta, N. (2002) Experimental and Numerical Investigation of Surface Treatment Effects on Turbine Blade Materials. *Surf Engineering*, **18**, 191-198.

[46] Lee, K. and Park, J. (2001) Thermal Stress and Fatigue Life Analysis of Francis Turbine Blades. *International Journal of Fatigue*, **23**, 41-47.

[47] Zhang, M. and Wang, Y. (2000) Coupled Thermal and Structural Analysis of Francis Turbine Blades Made of Advanced Materials. *Journal of Thermal Stresses*, **23**, 163-176.

[48] Li, W. and Xu, J. (2025) Investigation on Cavitation Characteristics and Material Erosion of Francis Turbine Blades. *Journal of Hydraulic Engineering*, **151**, Article 04024005.

[49] Chen, T. and Zhou, Q. (2024) Numerical Simulation of Cavitation and Flow Characteristics in Francis Turbine Runners. *Renew Energy*, **192**, 608-619.